Spectrophotometry of a Flare on EQ Pegasi A

Robert K. Buchheim
8731 E Lost Gold Circle, Gold Canyon, AZ 85118; Bob@RKBuchheim.org

Received December 30, 2025; revised April 6, 7, 2026; accepted April 10, 2026

Abstract Time-series B-band and TESS photometry is combined with time-series spectroscopy to characterize the brightness profile and the development of spectral features of a large flare on EQ Peg A. At its peak, the flare increased the star's brightness by 1.2 magnitudes in B-band, and it released ≈ 3.2×10^{32} erg in B-band. Photometrically, the flare showed a typical "fast rise, exponential decay" shape, with FWHM ≈ 1.7 minutes. Time-series spectroscopy shows that the Balmer emission lines remain strong for a much longer time (FWHM ≈ 11 to 15 min, depending on the line), taking about 3.5 hours to return to their pre-flare strength. The continuum slope of the flare spectrum indicates a peak temperature of $T_{Flare} = 14{,}000\,K \pm 2000\,K$ (averaged over a 5-minute exposure). The photometric color index (B-TESS) indicates a peak color temperature of $T_{(B\text{-}TESS)} \approx 11{,}800\,K$.

1. Introduction

Stellar flares occur randomly and relatively rarely. The concept for this project is that amateur astronomers can devote much more time to observing flare stars than can realistically be done by professional astronomers. Despite our modest equipment, we can probably make useful contributions to characterizing the photometry and spectroscopy of flares and adding to the collection of data about them. EQ Peg A was on our observing plan during TESS Sector 56, during which the target was within the TESS field of view.

EQ Peg (= GJ 896 = HIP 116132 = AAVSO UID 000-BCW-694, R.A. $23^h\ 31^m\ 52^s$, Dec. +19° 56' 14" (J2000)) is a well-known red dwarf flare-star. It has a large proper motion (nearly ≈ 0.6 a-s / yr), so its actual place in the sky will be noticeably different from your star chart. EQ Peg A and B comprise the visual binary star WIR 1AB whose orbit has a semi-major access of a ≈ 5.5 a-s and orbit period of P ≈ 229 y (Hartkopf *et al.* 2001). An exoplanet (designated as GJ896 Ab) has been reported in orbit around the A star (Curiel *et al.* 2022). At the time of the observations reported here, EQ Peg B (≈ 12th magnitude according to SIMBAD) was separated by about 5.4 a-s.

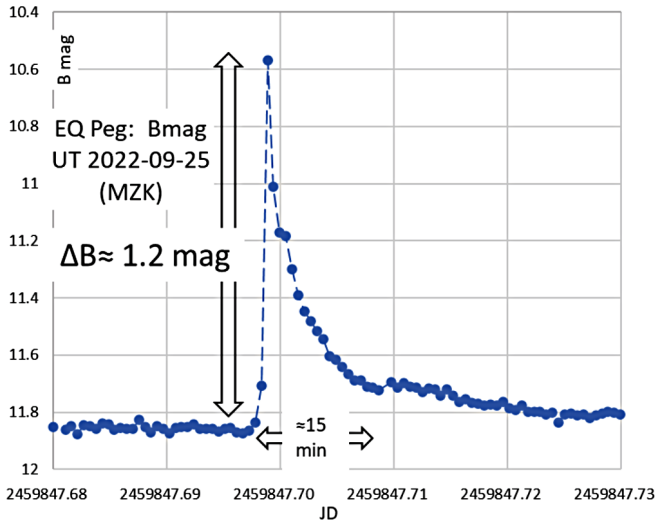

Figure 1. B-band photometry of the flare on EQ Peg.

EQ Peg was one of the targets of an ongoing project by a group of amateur astronomers (the "Red Dwarf Group") to characterize stellar flares with simultaneous spectroscopy and photometry. Both EQ Peg A and B have been reported as flare stars (Owen *et al.* 1972); the flare reported here occurred on the brighter component (EQ Peg A).

2. Observations

Here I present the optical (B-band) photometry, TESS space-based near-IR photometry, and optical band low-resolution spectroscopy of the flare. The optical data are freely available from the AAVSO's databases: photometry on the AID (Kloppenborg 2026a) and the spectroscopy on AVSpec (Kloppenborg 2026b). Near-infrared photometry from TESS can be freely downloaded via the lightkurve package (Lightkurve Collaboration 2018).

2.1. B-band photometry

Time-series photometry was done using a Hyperion CDK 12.5" f/8 Telescope and SBIG STL6303e camera with Johnson B-band filter. A continuous series of images were taken with 30 s exposure (and about 16 s image download time), with 2 × 2 binning yielding an image scale of 1.46 a-s / pix (binned). Aperture photometry used AAVSO's VPhot package, with star / gap / sky radii of 4 / 8 / 16 pix (= 5.8 / 11.7 / 23.4 a-s). The comparison star used was TYC1723-69-1 (AAVSO ID = 000-BNZ-811) with assigned $B_{mag} = 11.796$ (B–V = 0.972). The faint component of the visual double was touching the edge of the star aperture, so there is probably some contamination from it in the photometry. No adjustment was made for this.

EQ Peg A's light curve in Figure 1 shows the dramatic brightening (delta-mag 1.2 in B-band, briefly tripling the star's luminosity) and characteristic flare profile of "Fast Rise, Exponential Decay." The event is quite brief—it is nearly over in just 15 minutes, and the FWHM is much shorter than that.

The B-band photometry cadence barely resolves the rapid rise and fall of the event. Tovar Mendoza *et al.* (2022) developed a parametric model flare profile, based on a statistical analysis of a large sample of photometrically observed stellar flares, and a Python code that finds the model parameters (time of peak flux, FWHM, and peak amplitude) that fit a data set.

The Tovar Mendoza model fits the B-band photometry of this flare quite well, as shown in Figure 2. The model fit result for the FWHM of this flare is just 1.65 minutes.

2.2. TESS space-based near-infrared photometry

The Transit Exoplanetary Survey Satellite (TESS; Ricker *et al.* 2015) photometry cameras have a very broad spectral response in the red/near-IR (spanning about 5800 Å to 10,000 Å). The TESS pixels are very large (≈21 a-s), so the companion star EQ Peg B is almost certainly included in the TESS flux. The AAVSO VSX (Watson *et al.* 2006) lists the "A" component as V = 10.38 and spectral type M4Ve, and the "B" component as V = 12.58 and spectral type M6Ve, implying a contamination amounting 12% of the total flux in V-band. However, the spectral types indicate the "B" component will be relatively brighter in the red/near-IR TESS band, leading to a possible contamination that could be as much as 23% of the total flux (based on spectral profiles for the two types from Pickles 1998). No adjustment for this was attempted in our analysis.

The TESS data for Sector 56 were downloaded using the lightkurve tool. The results reported here use the PDCSAP flux (which has common instrumental systematics removed). TESS PDCSAP flux ($e^- s^{-1}$) was converted to TESS magnitudes ("T_{mag}" hereafter) using the information in Vanderspek *et al.* (2018), which gives (Equation 1):

$$T_{mag} = -2.5 \log (S) + ZP , \quad (1)$$

where S is the TESS signal flux in $e^- s^{-1}$ and the zero-point is ZP = 20.44.

In the TESS band, the star is quite bright, and the delta-magnitude of the flare is much smaller than it is in the B-band. The flare created less than a tenth of a magnitude increase in the TESS band brightness, as shown in Figure 3.

The app of Eastman *et al.* (2010) was used to convert the time scales of the ground-based photometry and TESS photometry to BJD. The flare brightness peaks in the two bands are: B photometry peak data point = JD (UTC) 2459847.69885 = BJD 2459847.70501; TESS 20s cadence peak data point = BJD 2459847.705153.

The difference between the two is ≈ 12 sec, which is essentially simultaneous considering the 20-s cadence of TESS and 46-s cadence of the B-band photometry.

The full TESS Sector 56 light curve of EQ Peg A is shown in Figure 4. The exquisite precision of TESS photometry shows that the star's brightness fluctuates by about 3% (full range) in a regular cycle. The most likely cause of the brightness cycle is rotational modulation, driven by a pattern of star-spots. Quite a few flares are obvious in this plot; our flare is indicated by the red box.

Norton *et al.* (2007) determined EQ Peg A's rotation period to be 1.066 d from SuperWasp photometry; Morin *et al.* (2008) reported a rotation period of 1.061 d from Zeeman-Doppler imaging. A PDM analysis of the TESS Sector 56 PDCSAP flux using PERANSO software (Paunzen and Vanmunster 2016) gives a modulation period of P = 1.06767 d—consistent with Norton *et al.* (2007) but slightly different than Morin *et al.* (2008). Figure 5 shows the TESS light curve phased to rotation period P = 1.06767 d. The red arrow points to our flare. A qualitative

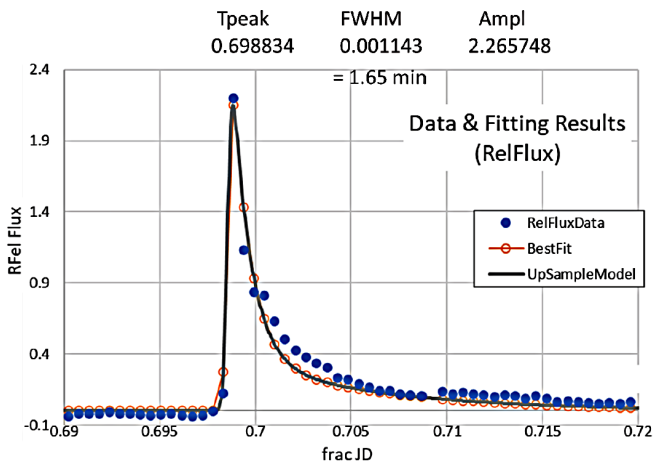

Figure 2. Best fit of Mendoza *et al.* (2022) model flare parameters to the B-band photometry of the flare on EQ Peg A.

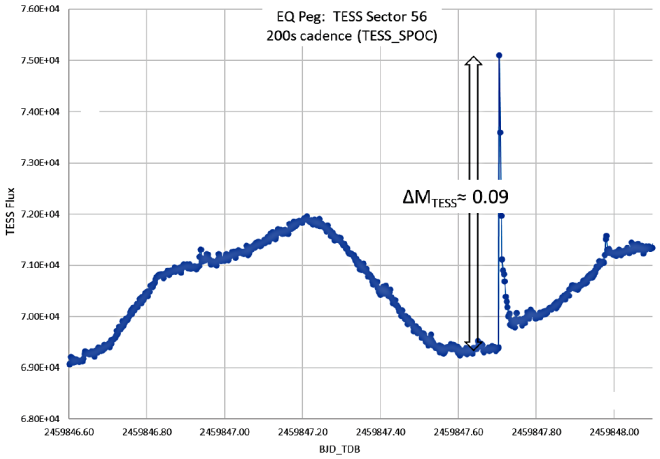

Figure 3. TESS light curve of EQ Peg at the time of our observations of the flare.

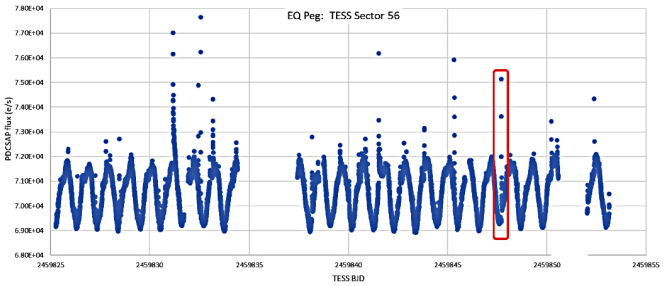

Figure 4. TESS Sector 56 light curve of EQ Peg, showing cyclic modulation punctuated by flare events. The red box indicates the flare that is the subject of this paper.

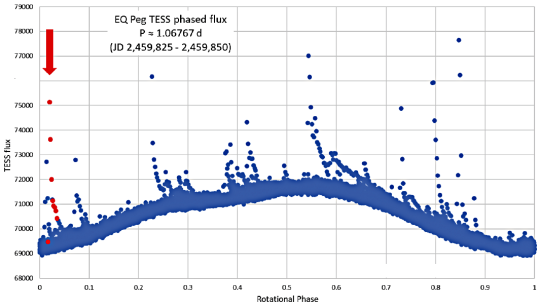

Figure 5. TESS Sector 56 light curve of EQ Peg, phased to stellar rotation period P = 1.06767 d. The red arrow points to the flare that is the subject of this paper.

look at this compilation of 22 observed rotations does not seem to show any obvious preference for flares to occur (or not occur) at particular rotational phases. This is consistent with the results of other studies, such as Hawley *et al.* (2014) and Zhang *et al.* (2025). Pratt *et al.* (2026) reported evidence for a small statistical preference for flares to be bunched ("sympathetic flares"), but did not see a correlation between flares and stellar rotational phase.

2.3. Optical low-resolution time-series spectroscopy

Time-series spectroscopy used a Shelyak ALPY spectrograph (R ≈ 500) with an ATIK 314L+ camera, on a 16-inch RC telescope. The spectra cover the spectral range λλ ≈ 3750 Å to 7250 Å. The instrument uses a 23 µm slit (= 1.45 a-s width), with the along-slit direction oriented East-West (i.e. perpendicular to the parallactic angle). The companion star EQ Peg B was clearly outside of the slit, as shown in the guider image in Figure 6, and there is no evidence of contamination by it in the spectrum images. Wavelength calibration is provided by a Ne-Ar lamp. Lamp images were taken at the start of the all-night run, and again after meridian-flip. There is a slight calibration-shift (most likely due to instrument flexure and temperature change), amounting to 1.5 Å over the night. The custom code that calculates emission line Equivalent Width accounts for this by shifting the observed wavelength of each line to its laboratory wavelength as part of the computations. Spectra of a Reference Star (HD 220933) were taken at large air mass (at the start of the observing run, elevation angle = 38 deg, AM ≈ 1.6) and low air mass (after meridian flip, elevation angle = 72 deg, AM = 1.05), and used to establish the Instrument+Atmosphere response function (spanning the full spectral range) for the night. Experience shows that this will create accurate and repeatable relative flux spectra over the full spectral range. However, this step is not by itself sufficient for flux-calibration of the spectra. For that, B-band photometry is used, as discussed in section 3.2.

Spectra were processing using the ISIS code by Christian Buil (2026), which handles dark subtractions, flat correction, sky subtraction, wavelength calibration, and correction for instrument response and atmospheric extinction, yielding an exo-atmospheric relative-intensity spectrum. An all-night (8.7 hr) observing run collected 93 spectra at a cadence of about one spectrum every 5.1 minutes (300-s exposure and about 10 s download time for each spectrum). This cadence under-samples the impulsive rise and rapid fall of the photometric flare, but provides a useful view of the evolution of spectral features from pre-flare quiescence to flare peak, and through the long fade back to quiescence. Since the sensitivity of the camera is relatively poor in the blue region and the target star is very red, the signal to noise ratio in the (pseudo) continuum is strongly wavelength dependent; it ranges from SNR ≈ 8 at Ca II (K) (3933 Å) to SNR ≈ 20 at H gamma (4340Å) to SNR ≈ 120 at H alpha (6563 Å).

Figure 7 shows the Relative Intensity spectrum of the star before the flare began: a normal M4 dwarf spectrum, aside from the fact that it shows emission in the Balmer and Ca II (K) lines, hence its spectral type "M4Ve."

Figure 8 shows the Relative Intensity spectra at three points in time: the quiescent state before the flare began, the spectrum that captured the peak of the flare, and a spectrum taken during the decay phase.

The sequence clearly shows the strong increase in the Balmer emission lines and the Ca II (K) line, plus the appearance of He I emission lines during the flare.

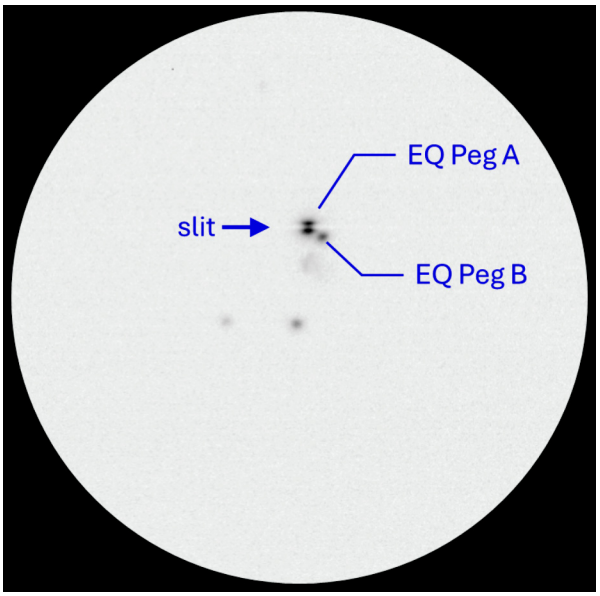

Figure 6. Guider image showing EQ Peg A on the spectrograph slit, and the companion EQ Peg B off of the slit. North is down and East to the right.

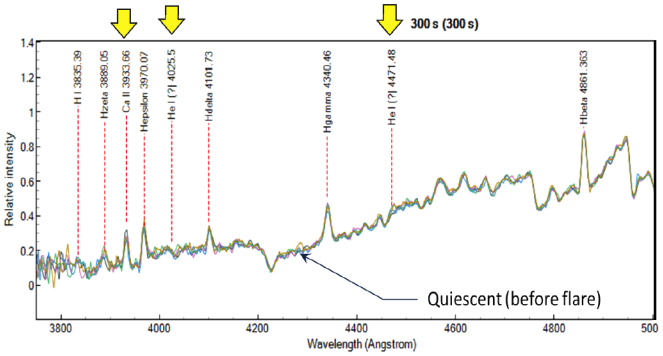

Figure 7. Spectra of EQ Peg during the "quiescent" state before the flare. This is an overlay of six spectra taken before the onset of the flare, showing the constancy of the quiescent spectrum over about 30 minutes before the flare (each spectrum exposure was 300 s).

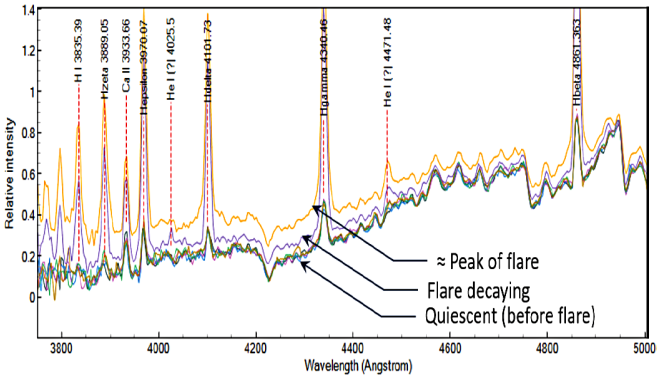

Figure 8. Changes in the spectrum near the peak of the flare, and during the photometric decay phase after the peak.

The Equivalent Width (EW) of a spectral line is a useful measure of the line's strength. Figure 9 shows the change in the strength of the H-alpha line during the flare, and compares it to the changing B-band brightness. The emission line peaks simultaneously with the B-band brightness, but stays elevated long after the B-band brightness has returned to its quiescent level. The H-alpha EW shows a hump interrupting its gradual decay from maximum strength (at about JD = 2459847.74). That hump is visible in the detailed photometric light curve. There is a similar, but very tiny, hump on the TESS light curve at the same time.

The long gradual decay isn't peculiar to the H-alpha line. All of the Hydrogen Balmer emission lines peak simultaneously and fall very gradually, as shown in Figure 10.

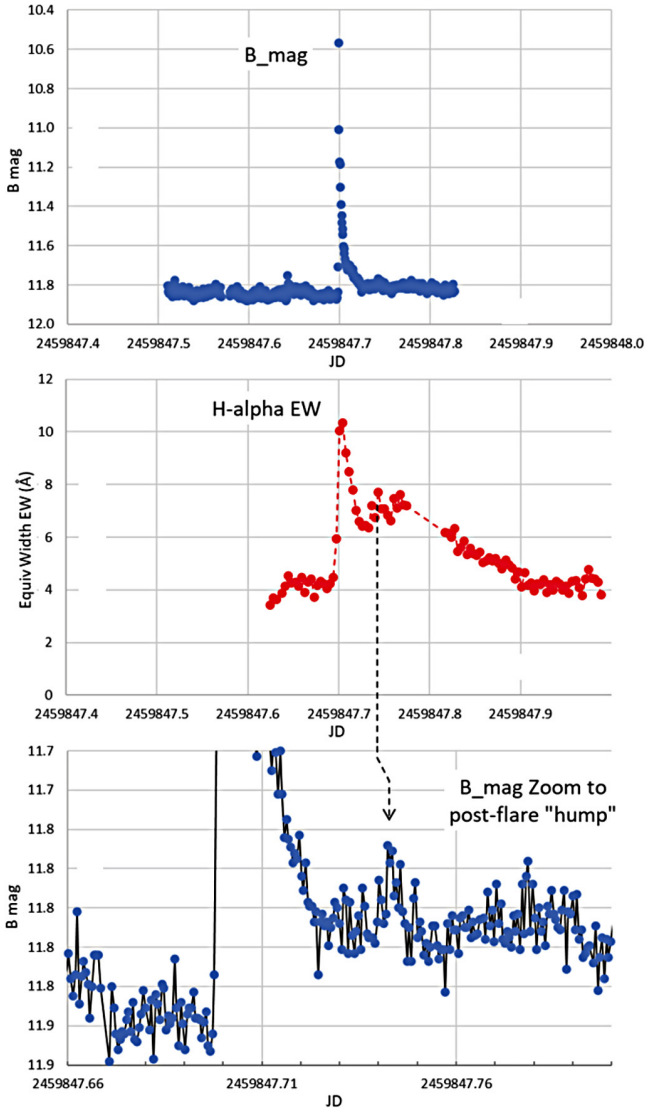

Figure 9. Comparison of H-alpha emission strength (Equivalent Width, Å) during the flare (middle graph) to the B-band brightness change (top graph). The hump that interrupts the decay of the H-alpha EW at 0.74 (dotted line) corresponds to a very small brightness hump in the photometry detail (bottom plot). The gap in H-alpha data is due to time lost during meridian flip.

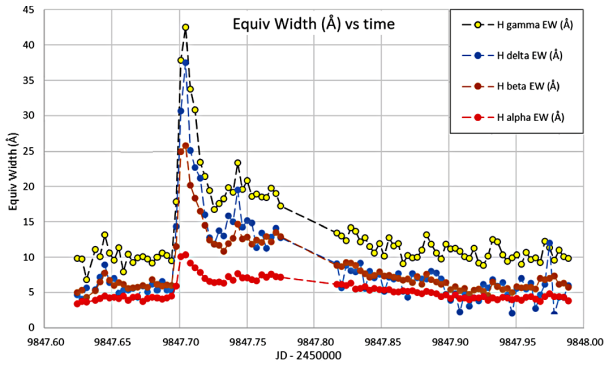

Figure 10. Strength of the Balmer H-alpha, H-beta, H-gamma, and H-delta lines during the flare, showing their gradual decays. The hump during the decline phase is seen on all of them. The gap in data (centered at about JD 2459847.80) is caused by meridian flip and reacquisition of the target.

3. Analysis

3.1. Photometry analysis

3.1.1. B-band

The luminosity (power emitted) of the flare is determined by a simplistic model, in which the flare is treated as a point source whose flux is added to that of the quiescent star. In this model, the observed luminosity is $L_{obs}(t) = L_Q + L_{Flare}(t)$. Writing the observation in terms of B-band magnitudes, and solving for the flare luminosity in B-band gives (Equation 2):

$$L_{Flare}(t) = L_Q \left[10^{-\left[\frac{(B_{obs}{}^{(t)} - B_{Q,Tgt})}{2.5}\right]} - 1 \right] (\text{erg S}^{-1}) , \qquad (2)$$

where $B_{obs}(t)$ is the observed B-magnitude at time t (i.e. star + flare), $B_{Q,Tgt}$ is the B-magnitude of the star during quiescence (no flare), L_Q is the quiescent luminosity of the star (erg s^{-1}) in the B-band, and $L_{Flare}(t)$ is the luminosity of the flare (alone) vs. time.

Treating the flare as a point source is justified by results such as Bicz *et al.* (2025) who analyzed a sample of flares from EV Lac and V374 Peg and found that the flare area was a very small fraction of the stellar surface (the maximum value they found for AFlare was less than 1% of the stellar surface, and their median value was 0.04%).

The quiescent luminosity of the star (L_Q) is found by determining the absolute magnitude of EQ Peg in B-band, in quiescence (Equation 3):

$$M_{Q,B,Tgt} = B_{Q,Tgt} + 5 \log(\pi) + 5 , \qquad (3)$$

where $\pi = 0.162$ a-s is the star's parallax (from SIMBAD), and comparing the target with the Sun's absolute magnitude and luminosity in B-band using the magnitude equation (Equation 4):

$$M_{Q,B,Tgt} - M_{B,\odot} = -2.5 \log \left(\frac{L_{Q,B,Tgt}}{L_{B,\odot}} \right) \qquad (4)$$

to solve for the target's quiescent luminosity. The absolute magnitude ($M_{B,Sun}$) and luminosity ($L_{B,Sun}$)of the Sun in B-band

(and many other photometric bands) are given by Willmer (2018) : $M_{B,\odot} = 5.44$, and $L_{B,\odot} = 5.008\,E+32$.

For EQ Peg A, the average B-mag observed over the 30 minutes preceding the start of the flare was $B_{Q,Tgt} = 11.855$ ($\sigma = 0.01$), so its quiescent Absolute Magnitude in B-band is $MB_{,Q,Tgt} = 11.855 + 5\log(0.162) + 5 = 12.903$.

The resulting quiescent luminosity of EQ Peg A is $L_{Q,EQPeg,B} = 5.18 \times 10^{29}$ erg s^{-1} in the B-band. Integrating over the duration of the flare (refer back to Figure 1) gives the total energy released as $E_B \approx 3.2 \times 10^{32}$ ergs in B-band.

3.1.2. TESS band

A similar procedure is used to analyze the flare luminosity and energy released in the TESS band. The average quiescent magnitude over the 30 minutes preceding the flare in the TESS band is $T_Q = 8.34$. The TESS light curve was essentially constant ($\sigma = 0.0006$ mag) over this time interval.

Willmer (2018) does not cover the TESS band, so his method and equations were followed to compute the Sun's absolute magnitude and luminosity in the TESS band, using the flux-calibrated solar spectrum from CalSpec (Bohlin *et al.* 2014), and the TESS spectral response function from Vanderspek (2018). The results are $M_{TESS,\odot} = 4.227$ and $L_{TESS,\odot} = 1.148\ E+33$.

The resulting quiescent luminosity of EQ Peg A in the TESS band is $L_{TESS,EQPegA} = 1.00\,E+31$ erg s^{-1}.

The star is much brighter in the TESS band than it is in the B-band, so despite the small delta-magnitude, the energy released by the flare in the TESS band was $\approx 6.6 \times 1032$ erg—more than twice as much as in the B-band.

3.1.3. Flare color-index and color temperature

The preceding analyses yield flare luminosity (erg s^{-1}) vs. time in both B- and TESS-band, which can be combined to estimate the blackbody color temperature of the flare. A two-step procedure was used. In step 1, Planck functions for an array of blackbody temperatures were integrated over the B- and TESS-bands using Equation 5,

$$L_{band}(T) = \int B(\lambda,T)\,R_{band}(\lambda)\,d\lambda\,, \qquad (5)$$

where $B(\lambda,T)$ is the Planck function vs wavelength at temperature T and $R_{band}(\lambda)$ is the normalized response curve of the photometric band (B- or TESS-band).

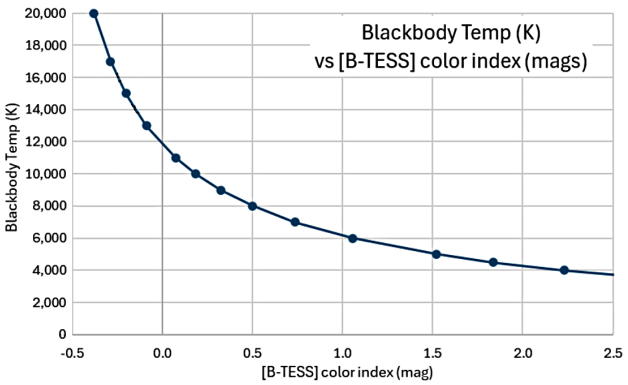

Figure 11. Blackbody (B-TESS) color index for Temperatures relevant to stellar flares.

For each blackbody temperature, the photometric color index was determined using Equation 6:

$$[B - T] = -2.5 \log\left(\frac{L_B(T)}{L_{TESS}(T)}\right). \qquad (6)$$

This was done for a range of temperatures that is relevant to stellar flares. The result is the curve shown in Figure 11.

In step 2, the TESS 20-s cadence data was interpolated to the time of each B-band data point, and the flare luminosity in the B- and TESS-band at each time point was used to compute the observed color index (in magnitudes), which was used with the data from Figure 11 to estimate the flare color temperature. This approach is identical to that used by Howard *et al.* (2020), except that they worked in flux ratio instead of color index magnitudes. The results are shown in Figure 12. The flare temperature spikes to $T_{BB} \approx 11800$ K, and then promptly falls to $T_{BB} \approx 8000$ K, before beginning a long gradual cooling as the flare luminosity fades.

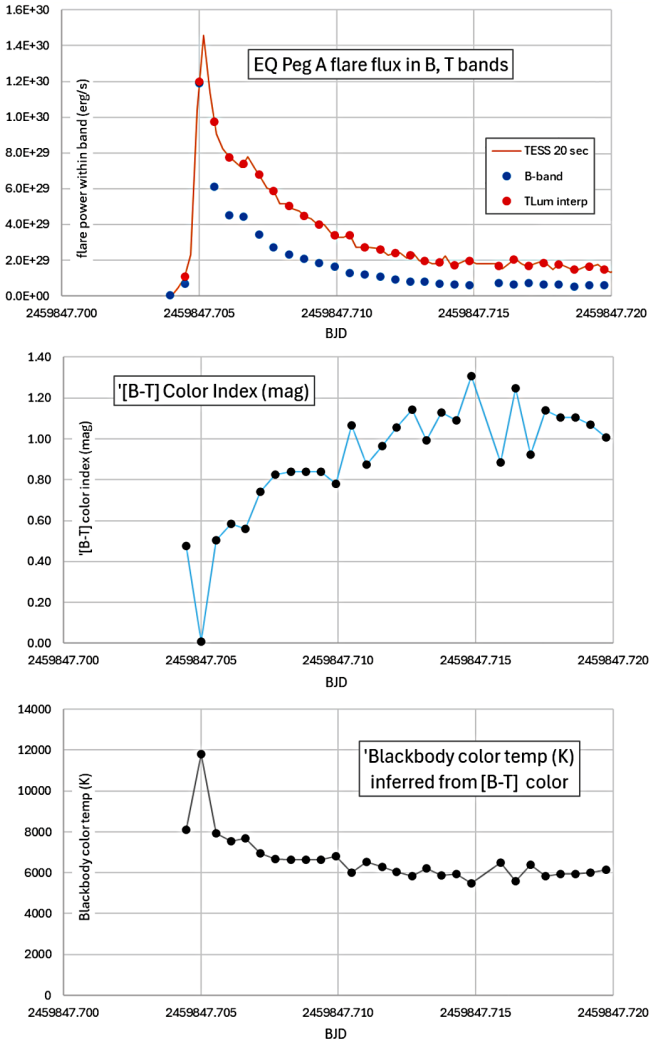

Figure 12. Determination of photometric blackbody temperature evolution of the flare. The top frame shows the flare power (luminosity, erg s^{-1}) in the B- and TESS- photometric bands. The middle frame shows the (B-TESS) color index (in magnitudes), and the bottom frame shows the inferred photometric blackbody temperature of the flare.

Howard *et al.* (2020) saw similar temperature evolution in their flares, although (not surprisingly) every flare has its own peak temperature and decay time-scale. Bicz *et al.* (2025) used a somewhat different method with B-band and TESS-band photometry to determine peak temperatures of a collection of flares on different stars. They found peak temperatures ranging from 5,700 K to 31,500 K—so the peak temperature reported for our flare is well within this range—and confirmed that the flare area is a very small fraction of the surface area of the star.

3.2. Flux-calibrating the spectra

A wonderful thing about having simultaneous photometry and spectroscopy is that the photometry can be used to flux-calibrate the spectra, using the method of Boyd (2023). The magnitude of a star is related to the integral of the star's spectral flux over a passband of interest. For example, if we focus on the B-band, and use Vega as the standard star ($B_{Vega} \approx 0.0$), then

$$B_{star} - B_{Vega} = -2.5 \log \frac{[\int_0^\infty [F_{star}(\lambda)] * R_b(\lambda)\, d\lambda]}{[\int_0^\infty [F_{Vega}(\lambda)] * R_b(\lambda)\, d\lambda]} . \quad (7)$$

Equation 7 is just another way of writing the definition of the magnitude system, where F_{star} and F_{Vega} are the flux-calibrated spectra of the target star and of Vega, and $R_b(\lambda)$ is the B-band response function.

The normal spectrum processing (e.g. using the ISIS software) yields only a relative flux spectrum $f_{star}(\lambda)$, normalized by the spectral processing pipeline. We then assume that the flux-calibrated spectrum of our target star is related to its relative flux spectrum by a factor K, such that Equation 8 holds:

$$F_{star}(\lambda) = K \cdot f_{star}(\lambda) \quad (8)$$

Since we have an independent photometric measurement of the B mag of the target from simultaneous photometry, we can solve Equation (8) for the K-factor that converts the relative flux spectrum of the target star into its fluxcalibrated spectrum, given by Equation 9:

$$K = \frac{10^{\left(\frac{ZP - B_{star}}{2.5}\right)}}{\int_0^\infty f_{star}(\lambda) * R_b(\lambda)\, d\lambda} \quad (9)$$

B_{star} is the observed B-mag of the star as a function of time, so K is also a function of time. The zero point comes from the flux-calibrated spectrum of Vega, using Equation 10:

$$ZP = B_{Vega} + 2.5 \log \left[\int_0^\infty F_{Vega}(\lambda) * R_b(\lambda)\, d\lambda\right] . \quad (10)$$

A custom Python code was written to integrate the B-band photometry over the exposure duration of each spectrum, calculate the K-factor, and output the flux-calibrated spectrum corresponding to each relative-flux spectrum. In this way, the time-series of relative-flux spectra is translated into a time-series of flux-calibrated spectra of EQ Peg A, showing the evolution of star's spectral flux.

The time-series includes a set of spectra made during the quiescent state of the star, before the flare began. If we assume that the flare is a flash of light coming from a tiny fraction of the star's surface, then what we observe during the flare event is quiescent star plus flare. This enables finding the flare-only spectrum by subtracting the quiescent "star only" spectrum from the "star plus flare" spectra. The flare-only spectra vs time, showing how the flare itself evolves, are determined using Equation 11:

$$F_{Flare}(\lambda,t) = F_{star}(\lambda,t) - F_{quiescent}(\lambda) \quad (11)$$

In practice, the quiescent spectrum was created from 6 spectra taken during the period prior to the flare, when the star's photometric B-band brightness was essentially constant. These were flux-calibrated, then averaged to yield $F_{quiescent}(\lambda)$.

The practical implementation of this approach is shown in Figure 13.

Considering the orientation of the slit (perpendicular to the parallactic angle, hence risking slit-function variations due to differential atmospheric dispersion, particularly in the blue end of the spectra), and the possibility of atmospheric changes over the duration of the flare, it is reasonable to be concerned about the reliability of such a treatment of the time-series spectra. Happily, the flare occurred when the target was very high in the sky, minimizing atmospheric effects. At the start of the flare, the elevation angle was 59° (airmass ≈ 1.17) and when the flare continuum (outside of the emission lines) returned to near-zero the elevation angle was 62° (air mass ≈ 1.09). Examination of the raw signal levels in the spectra images showed good consistency before and after the flare (no significant change in atmospheric conditions), and the flux-calibrated spectra during quiescence before the flare (see Figure 15 below) and 2 h after the flare show continuum levels that are essentially identical. So there seems to be no adverse atmospheric or slit function effects, and there was no attempt to compensate for such issues.

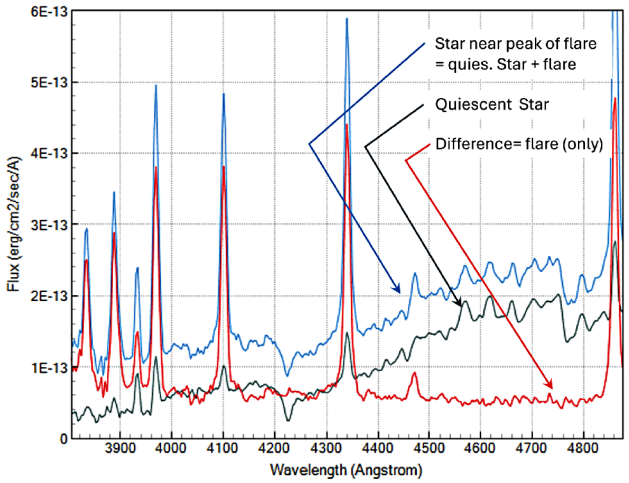

Figure 13. Example of the method of calculating the flare spectrum. All spectra are in flux-units (erg s^{-1} cm-2 $Å^{-1}$). The black line is the average quiescent spectrum of the star. The blue line is the spectrum of the star near the peak of the flare. The red line is the difference between the two – the spectrum of the flare itself.

3.3. Evolution of the flare spectrum

This discussion will concentrate on five spectra identified in Table 1: one showing the quiescent state, three that show measurable views of the flare continuum, and one that shows the sustained emission lines after the continuum has returned to nearly the quiescent level.

The times and weighted-average B-magnitudes of these spectra are shown in Figure 14, with symbols that reasonably illustrate the duration of the spectrum exposures compared to the B-band photometry points.

The next several Figures illustrate the flare evolution, comparing the flare spectral flux in the blue portion of the spectral range (top), a detail of the H-gamma line (2nd), the B-band photometry (3rd) and the H-alpha line equivalent width (bottom).

Figure 15 shows the Quiescent state (JD-MID = 0.6941)—the B-mag and the H-alpha Equivalent Width are at their quiescent levels, and the flare spectrum is a flat line at zero flux (aside from measurement noise).

Figure 16 shows spectrum taken during the rise to peak brightness of the flare: B-mag has started its rapid rise, H-alpha and all the Balmer lines have started their rapid rise, the flare continuum level has jumped up, and enhanced emission lines have appeared.

Figure 17 is the very next spectrum—5 minutes after Figure 16—spanning the rapid rise and the peak of the flare's B-band brightness. The flare spectrum continuum is only slightly elevated from the preceding spectrum, but the emission lines are much strengthened.

Table 1. Identification of flux-calibrated spectra.

JD-MID –2459847	*B mag*	*Comments*
.6941	11.857	Quiescent, before start of flare
.6976	11.460	Start of photometric rise
.7011	11.287	Peak of flare
.7046	11.595	Emission lines strong, continuum fading
.7081	11.704	Emission lines elevated, but continuum too noisy to estimate blackbody temperature

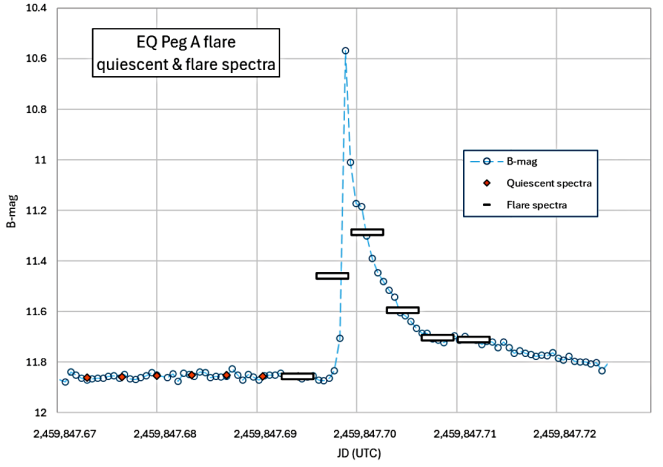

Figure 14. Spectra times and weighted-average magnitudes of flare spectra discussed in sections 3.1 and 3.2. Note the time-axis: this is a small portion of the overall photometry shown in Figures 15 through 19.

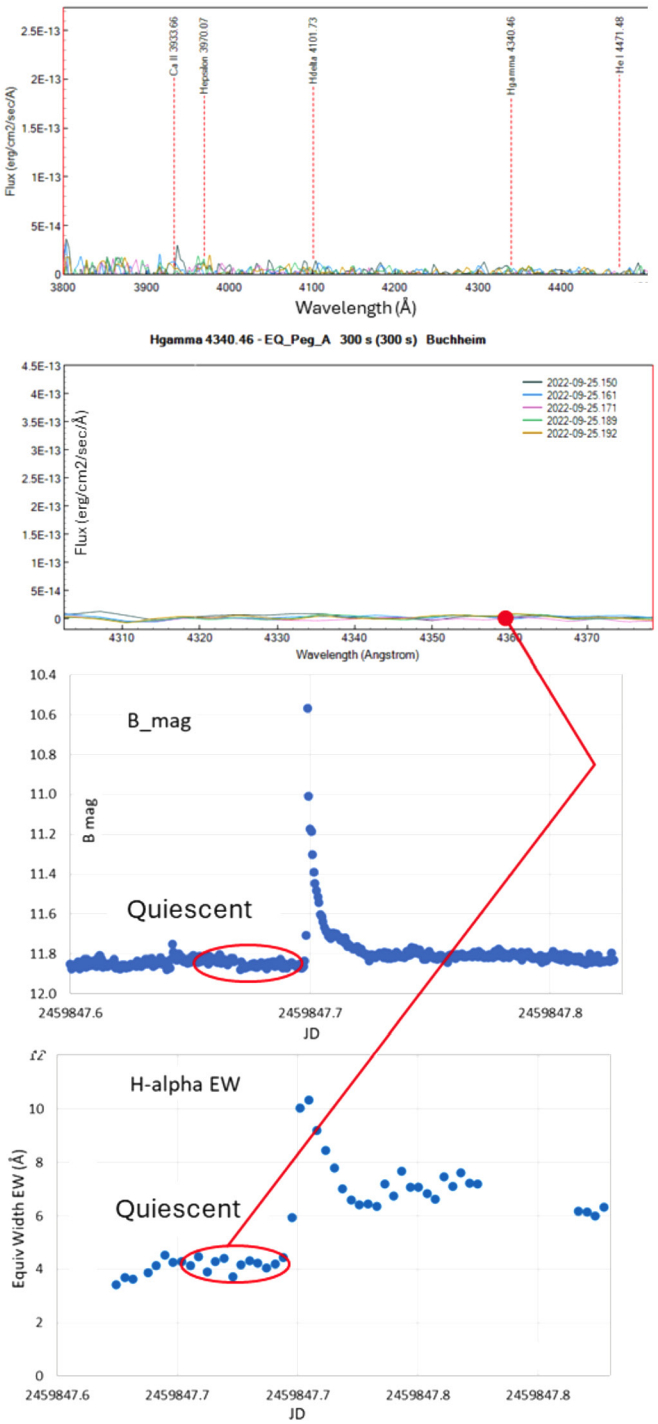

Figure 15. Flare spectrum in the quiescent state (pre-flare) at JD-MID = 0.6941.

Figure 18 spans most of the rapid fall in brightness. The flare continuum has dropped almost to its quiescent level, but the emission lines are still very strong. Note that the wings of the emission lines were significantly broadened during the flare, but they are now shrinking back to their normal width.

In Figure 19, when the photometric flare is just about over, the continuum is indistinguishable from the quiescent level, but emission lines are still elevated.

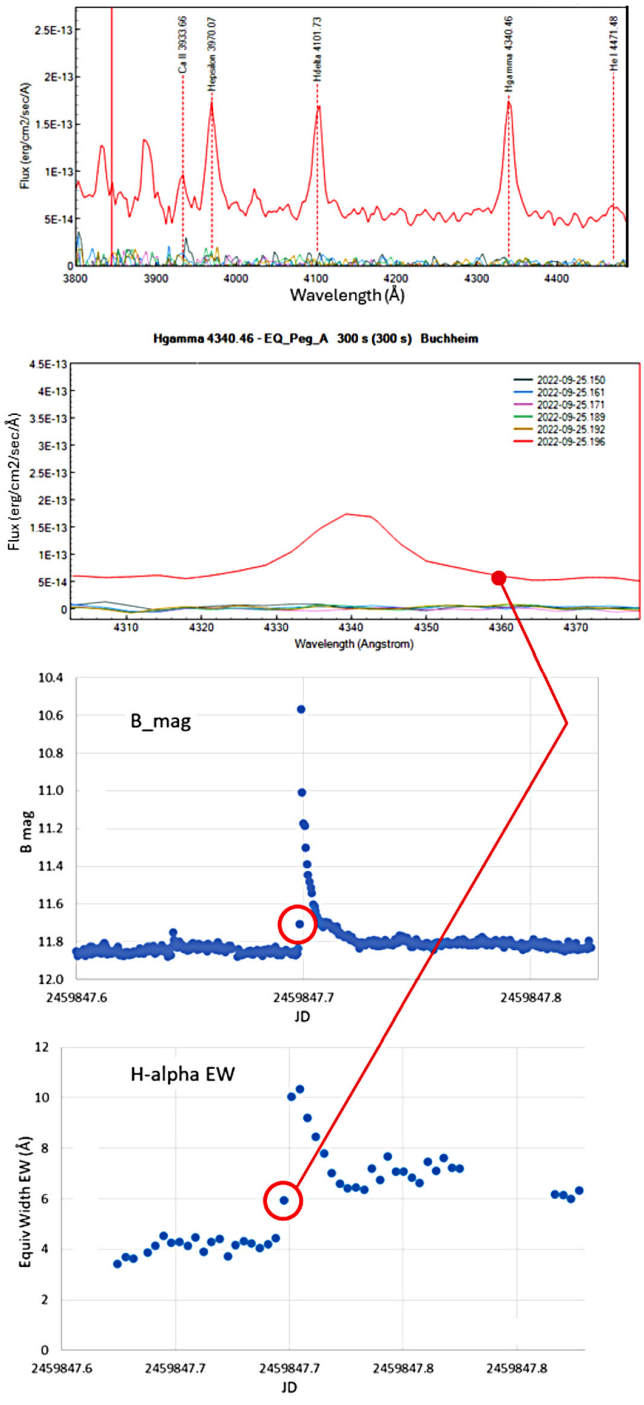

Figure 16. Flare spectrum at the very beginning of the flare, at JD-MID = 0.6976.

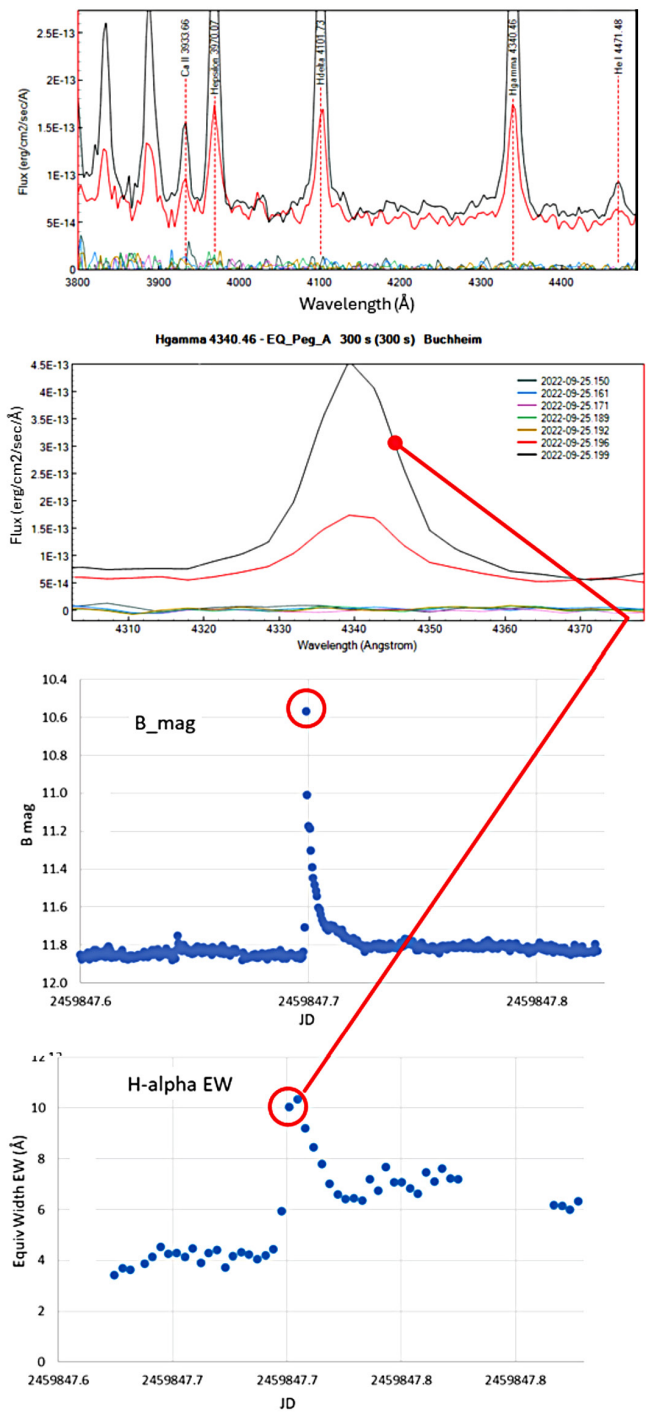

Figure 17. Flare spectrum at the peak of the flare at JD-MID = 0.7011.

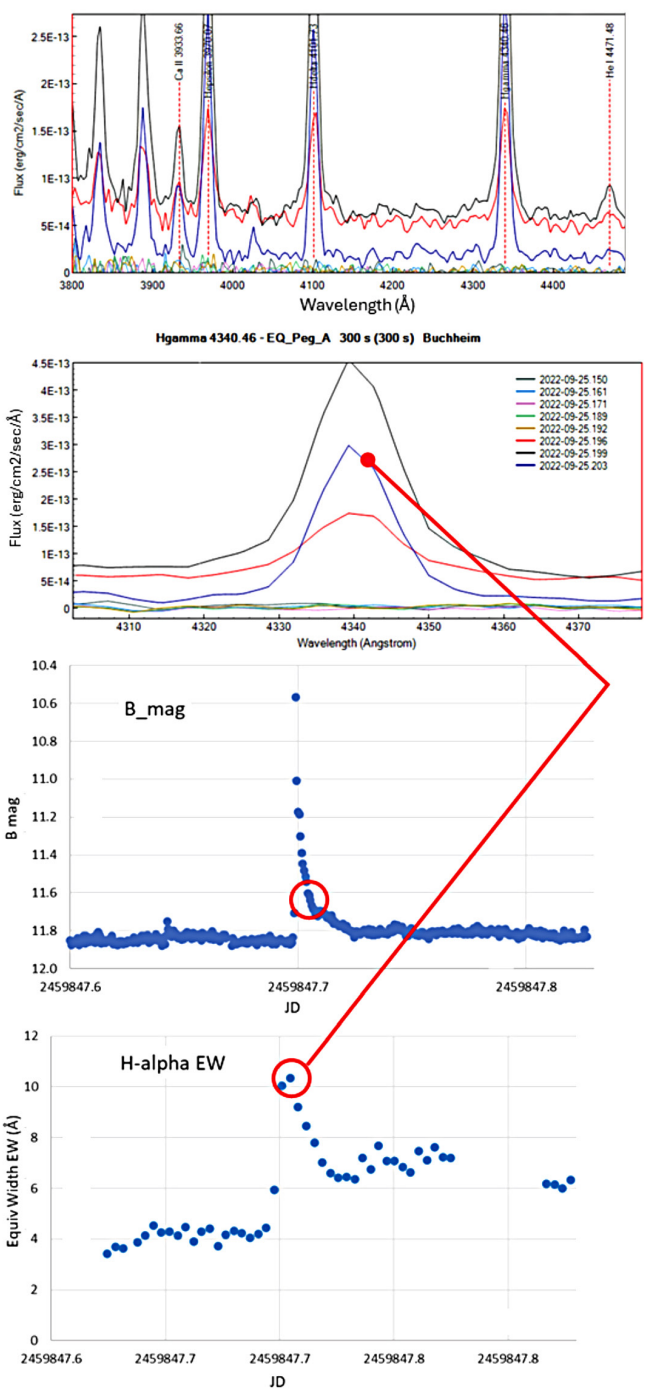

Figure 18. Flare spectrum during photometric decline at JD-MID = 0.7046. Note that the B-band brightness is nearing quiescence, but the H-alpha EW is still near its peak.

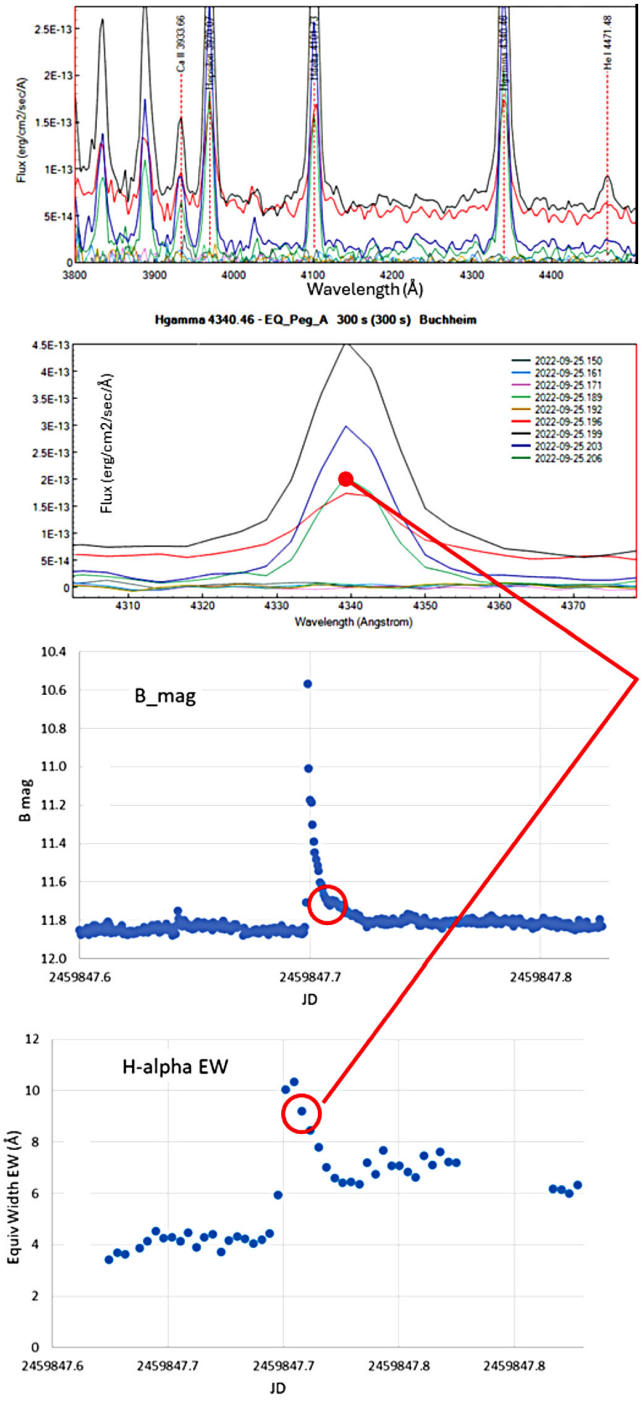

Figure 19. Flare spectrum at the end of the B-band flare at JD-MID = 0.7081.

3.4. Balmer line "time decrement"

The line flux vs. time of the bright emission lines is easily calculated from the flare-only spectra. The results are shown in Figure 20, for the Balmer lines and Ca II (K). There is a trend in the decay times ($t_{1/2}$ = the time to decay to 50% of the peak flux). As shown in Figure 21, the longer the wavelength, the longer it takes for the line to decay. This effect has been previously reported by Kowalski *et al.* (2013), who called it the Hydrogen Balmer "Time Decrement."

3.5. Flare continuum temperature

Kowalski *et al.* (2013) described an approach to fitting the continuum of the flare spectra to a Planck (blackbody) curve, yielding an estimate of the flare continuum temperature. They identified narrow regions that are relatively free of both absorption and emission features. Three of their continuum regions are within the spectral range of our spectra of EQ Peg A, and are defined in Table 2.

Considering the low resolution and modest SNR of the spectra, a sort of "estimation by eye" was applied, which will be illustrated using the example of the spectrum at the peak of the flare, JD-MID = 0.7011. A family of blackbody curves of plausible temperatures are first scaled so that they all match the flare spectrum and the "C4500" continuum. Figure 22 shows this in overview.

The detail of blackbody curves vs flare spectrum at C4500 is shown in Figure 23.

The same blackbody curves as they pass through continuum region C4170 are shown in Figure 24.

At C4170, the coolest Planck curves (6000, 7000 K) seem too low, and the hottest (12000, 14000, 16000 K) seem to be high, but probably shouldn't be ruled out at this point. The mid-range curves (8000, 10000 K) seem like fair fits to the continuum region, highlighted in grey.

A similar detail of the flare spectrum and blackbody curves at continuum region C6010 is shown in Figure 25.

Here, 7000 K and 8000 K blackbody curves seem to bracket the continuum region nearly perfectly. 6000 K is probably too high, and the curves for 10000 K through 16000 K are definitely too low. Considering this, and the picture at C4170, a fair estimate is that $T_{Flare} \approx 8000\,K \pm 2000\,K$ at this point in time.

A similar procedure was followed for the other flare spectra that showed a clear enough continuum for measurement. The resulting continuum temperatures are listed in Table 3.

These continuum temperatures are a bit higher than photometric color-temperatures at similar times shown in Figure 12, but qualitatively the trend is the same, and it is heartening that such similar temperatures are found from two different methods and two different wavelength regions. It seems that the initial burst of energy is the hottest, and the flare continuum continuously cools after this, while the emission lines remain elevated long after the continuum returns to its quiescent level. This result is similar to that seen in a flare on EV Lac by Ichihara *et al.* (2024).

3.6. Other emission lines

While the Balmer lines are most prominent in the flare spectrum, there are other weaker emission lines in the flare

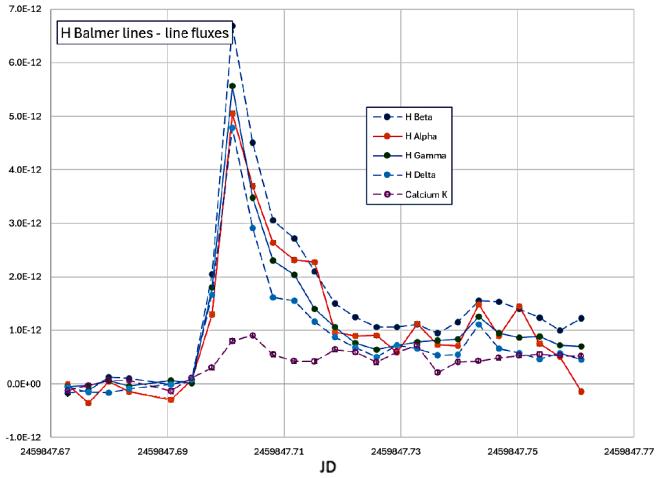

Figure 20. Balmer lines and Ca II (K) line flux vs time (flare-only).

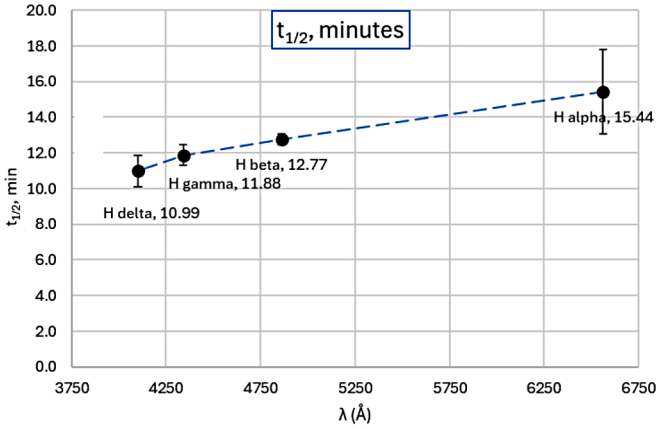

Figure 21. Balmer time decrement.

Table 2. Continuum regions used for fitting flare spectra to blackbody model (Planck function).

Continuum Measure	*Spectral Range (Å)*
C4170	4155–4185
C4500	4490–4520
C6010	5990–6030

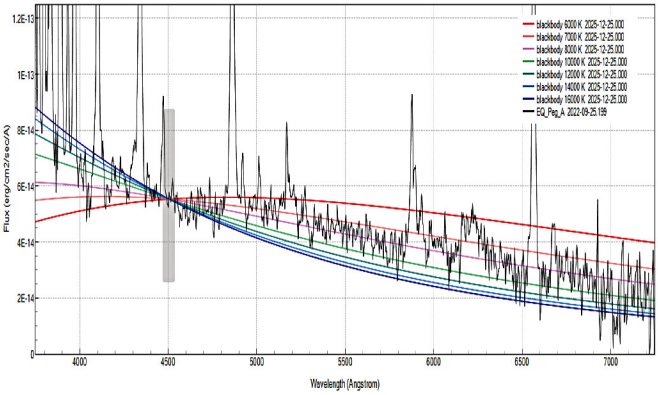

Figure 22. Overview of flare spectrum compared to blackbody spectra, scaled to match the flare at continuum spectral range "C4500" (highlight by grey rectangle).

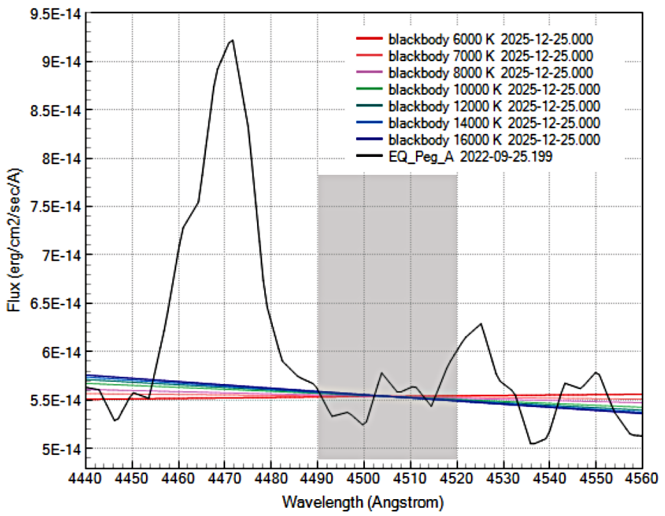

Figure 23. Blackbody curves passing through Continuum region C4500.

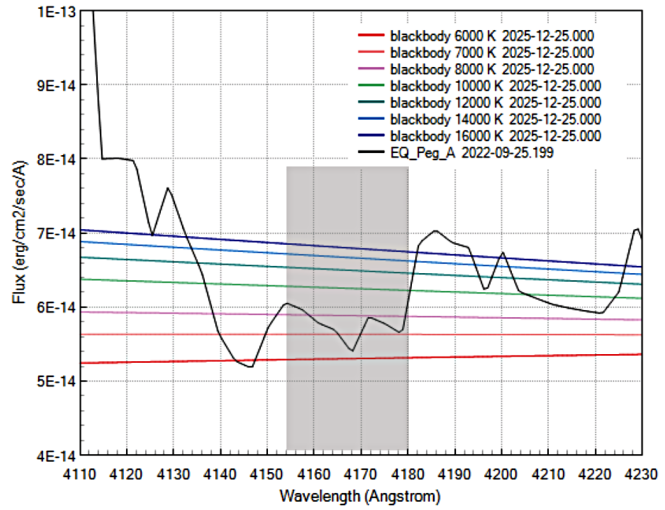

Figure 24. Blackbody curves passing through continuum region C4170.

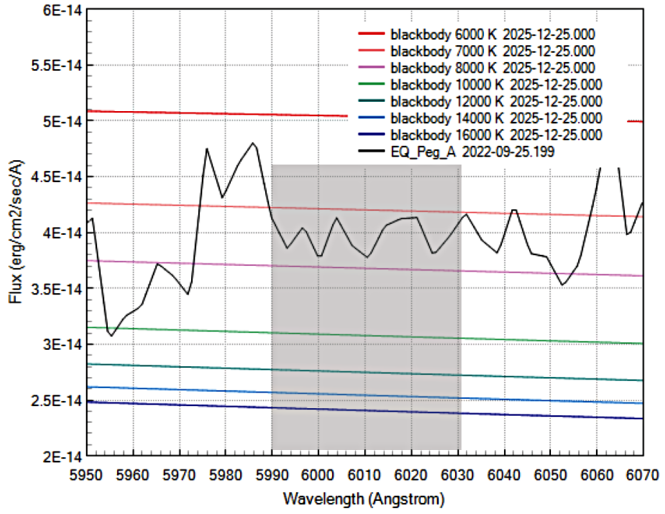

Figure 25. Blackbody curves passing through continuum region C6010.

Table 3. Evolution of flare spectrum continuum temperatures.

JD-MID –2459847	*B mag*	*T_{Flare} continuum temp (K)*
.6976	11.460	T_{Flare} = 14,000 ± 2000
.7011	11.287	T_{Flare} = 8000 ± 2000
.7046	11.595	T_{Flare} = 7000 ± 2000

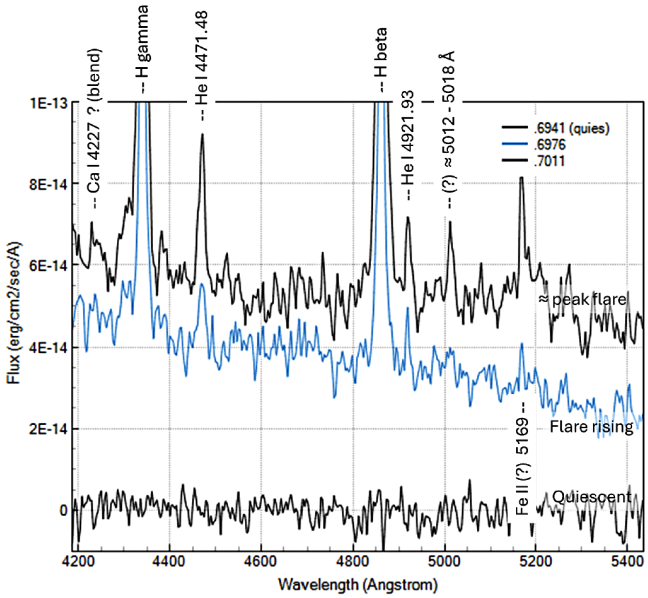

Figure 26. Detail of emission lines near H beta, at the start of the flare. Spectra are identified by their fractional JD: t = (JD – 2459847). The quiescent spectrum (t = .6941) taken just before the start of the flare is shown for comparison. The next spectrum is t = .6976, showing the rise of the flare, with the peak flare at t = .7011 at the top.

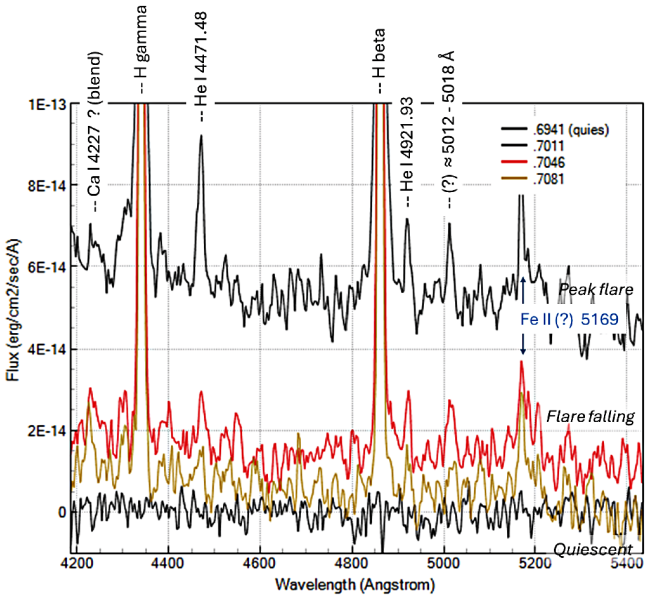

Figure 27. Continuum and emission lines changing as the flare fades from its peak.

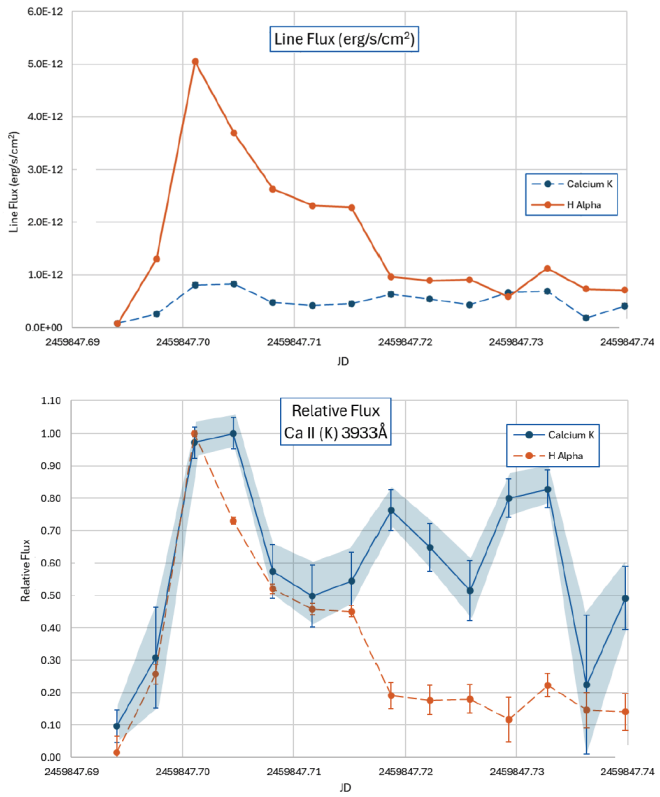

Figure 28. Line flux of the Ca II (K) emission line during the flare, with H alpha shown for comparison. The top graph shows the line strength in flux units. The bottom graph shows the same data, but with the flux normalized to the peak flux in each line. The signal level of Ca II (K) is low, and the spectrograph has low sensitivity to far-blue light (hence relatively poor signal to noise ratio), but the sustained strength of Ca II (K) seems to be real.

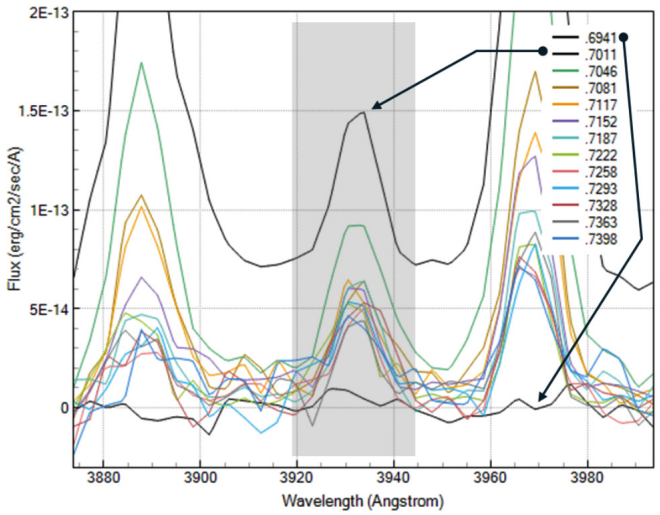

Figure 29. Detail of the time-series spectra in the Ca II (K) region (highlighted in gray), used for Figure 28. Spectrum ".6941" was taken just before the flare began, and provides a good view of the quiescent spectrum. Spectrum t =.7011 is the peak of the flare. The other curves show the spectra as the flare fades. The low SNR causing the wide scatter in the continuum region (left and right of line region) leads to "noise" in the line flux calculation; nevertheless, the sustained emission appears to be real.

spectrum. The first two spectra at the start of the flare are shown in Figure 26, illustrating the rise of several emission lines. The He I 4471 and He I 4922 lines appear promptly at the start of the flare. Abdul-Azis *et al.* (1995) suspected Ca I (4227 Å) emission during a flare on EV Lac. The Ca I 4227 line might be seen (as a blend) in the spectrum at JD-MID .7011 (peak of the flare), but it is weak or absent in the preceding spectrum at the very beginning of the flare, so its appearance—if real—is delayed compared to the Balmer and He I lines. Kowalski *et al.* (2013) saw a feature at ≈5018 Å which they suspected might be a blend of He I, Fe II or Mg Ib; the spectra here show a similar blended feature at the same location. A sharp bright line at 5169 Å is apparent in these spectra; Abdul-Aziz (1995) suggested that this might be Fe II (5169) or a blend with Mg I (5167, 5173).

Figure 27 is similar to Figure 26, except that it shows the spectra taken as the flare fades from peak. It highlights the possible strengthening of the Ca II 4227 (?) line, while the Fe II (?) 5169 feature stays strong as the flare fades.

The Ca II (K) line in flare spectra often displays a different time evolution than the H I and He I lines (e.g. Kowalski 2013; Buchheim 2022). In this flare, as shown in Figure 28, it sustained a strong emission far longer than the H alpha (and the other H I and He I lines) did. There is also a hint that it may have peaked later than the H-alpha line, by about 5 minutes.

The signal level is low, so the noise level and scatter in the Ca II (K) line flux data is large. Nevertheless, the trend of sustained Ca II(K) emission for longer than it is seen in the H I lines seems to be real. Figure 29 shows the evolution of the Ca II (K) spectral region for 55 minutes after the peak of the flare.

4. Conclusions

For targets like this, amateur observers have an asset that professional researchers don't: we can invest a great deal of observing time in hopes of seeing—and measuring—short-lived, rare events like stellar flares.

Simultaneous spectroscopy and photometry increases the information that can be derived from amateur and small-telescope observations. This applies not just to stellar flares, but also to many types of stellar variability and transients. The two techniques (photometry and spectroscopy) need not be done by a single observer. Teamwork between photometrist and spectroscopist is effective, even if they are geographically separated, as was the case for this project. The spectra were made in Arizona, and the B-band photometry was done in Massachusetts, but serendipitously two observers provided overlapping data on this flare.

The data show many flare features that have been reported by professional projects, which is heartening confirmation of the fidelity of the small-telescope results. Even in situations like this, where we may not be breaking new ground, achieving replication of prior—relatively rare—observations and conclusions is a contribution to science.

5. Acknowledgements

I acknowledge with thanks the variable star observations from the AAVSO International Database contributed by observers worldwide and used in this research.

This research has made use of the SIMBAD database, CDS, Strasbourg Astronomical Observatory, France (Wenger *et al.* 2000).

This research has made use of the VizieR catalogue access tool, CDS, Strasbourg Astronomical Observatory, France (Ochsenbein *et al.* 2000)).

This paper includes data collected with the TESS mission, obtained from the MAST data archive at the Space Telescope Science Institute (STScI). Funding for the TESS mission is provided by the NASA Explorer Program. STScI is operated by the Association of Universities for Research in Astronomy, Inc., under NASA contract NAS 5–26555.

This research made use of Lightkurve, a Python package for Kepler and TESS data analysis (Lightkurve Collaboration 2018).

This research made use of the program ISIS (Integrated Spectrographic Innovative Software; Buil 2026).

This research made use of Peranso (Vanmunster 2025), a light curve and period analysis software.

A hearty "thank you, and well-done!" to Ken Menzies and the other members of the Red Dwarf Group for their devotion to providing high-quality data in support of variable star investigations.

References

Abdul-Aziz, H. *et al.* 1995, *Astron. Astrophys., Suppl. Ser.*, **114**, 509.

Bicz, K., *et al.* 2025, *Astron. Astrophys.*, **699A**, 90.

Bohlin, R. C., Gordon, K. D., and Tremblay, P.-E. 2014, *Publ. Astron. Soc. Pacific*, **126**, 711.

Boyd, D., *et al.* 2023, *J. Amer. Assoc. Var. Star Obs.*, **51**, 14.

Buchheim, R. K., Sims, F., Curry, S., and Martin, J. 2022, in *Proceedings for the 41st Annual Conference of the Society for Astronomical Sciences (SAS-2022)*, eds. J. C. Martin, R. K. Buchheim, R. M. Gill, W. Green, J. Menke, The Society for Astronomical Sciences, Rancho Cucamonga, CA, 151.

Buil, C. 2026, ISIS Integrated Spectrographic Innovative Software (https://buil.astrosurf.com/isis-software.html).

Curiel, S., Ortiz-León, G. N., Mioduszewski, A. J., and Sanchez-Bermudez, J. 2022, *Astron. J.*, **164**, 93.

Eastman, J., Siverd, R., and Gaudi, B. S. 2010, *Publ. Astron. Soc. Pacific*, **122**, 935.

Hartkopf, W. I., Mason, B. D., and Worley, C. E. 2001, *Astron. J.*, **122**, 3472.

Hawley, S. L., Davenport, J. R. A., Kowalski, A. F., Wisniewski, J. P., Hebb, L., Deitrick, R., and Hilton, E. J. 2014, *Astrophys. J.*, **797**,121.

Howard, W. S., *et al.* 2020, *Astrophys. J.*, **902**, 115.

Ichihara, S., *et al.* 2025, *Publ. Astron. Soc. Japan*, **77**, 1025. [2025 not 2024]

Kloppenborg, B. 2026a, variable star observations from the AAVSO International Database (https://apps.aavso.org/v2/data/search/photometry/).

Kloppenborg, B. 2026b, AVSpec, variable star observations from the AAVSO Spectral Database (https://apps.aavso.org/avspec/search).

Kowalski, A. F., Hawley, S, L., Wisniewski, J. P., Osten, R. A., Hilton, E. J., Holtzman, J. A., Schmidt, S. J., and Davenport, J. R. A. 2013, *Astrophys. J., Suppl. Ser.*, **207**, 15.

Lightkurve Collaboration, Cardoso, J. V. M., *et al.* 2018, Astrophys. Source Code Libr. (https://ui.adsabs.harvard.edu/abs/2018ascl.soft12013L).

Morin, J., *et al.* 2008, *Mon. Not. Roy. Astron. Soc.*, **390**, 567.

Norton, A. J., *et al.* 2007, *Astron. Astrophys.*, **467**, 785.

Ochsenbein, F., Bauer, P., and Marcout, J. 2000, *Astron. Astrophys., Suppl. Ser.*, **143**, 23.

Owen, F. N. Bopp, B. W., Moffett, T. J., and Lazor, F. J. 1972, *Astrophys. Lett.*, **10**, 37.

Paunzen, E., and Vanmunster, T. 2016, *Astron. Nachr.*, **337**, 239.

Pickles, A. J. 1998, *Publ. Astron. Soc. Pacific*, **110**, 863.

Pratt, V., Reeves, J. R., Martin, D. V. Zhang, A. B. Korkus, A., and Edelman, S. 2026, arXiv:2602.20311v1 [astro-ph.SR] (https://doi.org/10.48550/arXiv.2602.20311).

Ricker, G. R., *et al.* 2015, *J. Astron. Telesc. Instrum. Syst.*, **1**, 014003.

Tovar Mendoza, G., Davenport, J. R. A., Agol, E., Jackman, J. A. G., and Hawley, S. L. 2022, *Astron. J.*, **164**, 17.

Vanderspek, R., Doly, J. P., Fausnaugh, M., Villasenor, J. N. S., Jenkins J. M., Berta-Thompson, Z. K., Burke, C. J., and Ricker, G. R. 2018, *TESS Instrument Handbook*, v0.1.[1]

Vanmunster, T. 2025, Peranso light curve and period analysis software (https://www.cbabelgium.com/peranso).

Watson, C. L., Henden, A. A., and Price, A. 2006, in The Society for Astronomical Sciences 25th Annual Symposium on Telescope Science, The Society for Astronomical Sciences, Rancho Cucamonga, CA, 47 (https://vsx.aavso.org/).

Wenger et al. 2000, *Astron. Astrophys., Suppl. Ser.*, **143**, 9.

Willmer, C. N. A. 2018, *Astrophys. J., Suppl. Ser.*, **236**, 47.

Zhang, A. B., Reeves, J. R., Martin, D. V., Pratt, V., Tubthong, W., Weinstein, A., and Ward, I. E. 2025, arXiv:2512.01051 (https://doi.org/10.48550/arXiv.2512.01051).

[1] Vanderspek *et al.* (2018): https://archive.stsci.edu/files/live/sites/mast/files/home/missions-and-data/active-missions/tess/_documents/TESS_Instrument_Handbook_v0.1.pdf